High-Frequency Aging Model Modeling Method of Passive Devices in EMI Filter Based on Electromagnetic Field Analysis

Wenzhe Su, *Student Member, IEEE*, Hong Li, *Senior Member, IEEE*, Changlin Ji, Zuoxing Wang, *Student Member, IEEE*, Xueyang Liu, and Baihua Zhang

***Abstract*—Power electronic devices must be certified for electromagnetic compatibility compliance before mass verification. However, this test does not consider the influence of aging factors, leaving hidden risks to electromagnetic compatibility. In this article, the passive device in the electromagnetic interference filter is taken as the research goal, and a lumped parameter high-frequency aging model with physical significance is established based on the electromagnetic field analysis. The proposed model has the ability to accurately describe the high-frequency characteristics of passive devices from 150 kHz to 30 MHz. At the same time, this article proposes a parameter extraction method for practical design. Based on the existing accelerated aging experiments, only one additional high-frequency characteristic measurement is required to predict the aging characteristics of passive devices. The proposed method achieves the prediction of high-frequency aging characteristics of passive devices within confidence intervals. Experiments verify the accuracy and correctness of the model, which can be applied to electromagnetic compatibility design considering aging.**

***Index Terms*—Aging prediction, electromagnetic field analysis, high-frequency aging models, passive component.**

I. Introduction

ELECTROMAGNETIC interference (EMI) emission compliance is a crucial part of product verification and a necessary step before mass verification [1]. The international standardization organization, countries, and enterprises have all implemented strict EMI emission standards and are committed to quantitatively, credibly, and repeatably measuring the EMI emitted by the device under test (DUT), so as to ensure that the electronic equipment in electric vehicles (EVs) will not be affected by EMI [2], [3]. Although the product has passed the EMI emission limit, the actual product may still have EMI problems after long-term operation. Such EMI issues are not limited to failures of EMI suppression caused by environmental electrical, thermal, and mechanical stress [3]. It can be seen that EMI design runs through the entire life cycle of power electronic products. It is very important to study the EMI design of the whole life cycle of power electronic equipment.

Motor drivers and vehicle-mounted dc–dc converters perform the high-power conversion in EVs and are among the power electronic devices most affected by aging. This is because the power electronic devices in EVs are designed in a confined space to cope with the complex driving environment, which will cause the power electronic devices to withstand high-temperature stress [4]. Passive components subjected to high temperature stress for a long time will experience performance degradation, which will lead to excessive EMI. Excessive EMI of motor controllers will affect the normal operation of surrounding equipment [5]. Currently, online EMI measured technology throughout the lifetime of the equipment for regulatory tests is being developed [6]. However, the current EMI test does not consider the influence of aging factors, which leaves hidden dangers of electromagnetic compatibility (EMC). Therefore, it is critical to study an EMI design method that considers the aging effects of passive components.

In the existing research, the aging models of capacitors are divided into ideal capacitor models [7], RC series models [8], [9], RC series-parallel models [10], [11], RC network models [12], [13], lumped parameter models [14], [15], and neural network based model [15], as shown in Fig. 1.

The inductors in passive filters can be divided into differential-mode (DM) inductors and common-mode (CM) inductors. Typically, DM inductors use the same model as normal inductors for the same construction. For CM inductors, the model is usually decomposed into a CM impedance model and a DM impedance model. The decomposed DM impedance model and CM impedance model have the same model as the normal inductor [16]. Many scholars have studied the impedance-frequency characteristics of inductors and proposed corresponding models [17], [18], [19], [20], [21], as shown in Fig. 2. However, there are few studies discussing the law of inductor impedance-frequency aging transformation in passive filters.

Manuscript received 8 March 2023; revised 12 July 2023; accepted 7 August 2023. Date of publication 22 August 2023; date of current version 23 October 2023. This work was supported in part by the Excellent Youth Scholars of the National Natural Science Foundation of China under Grant 51822701, and in part by the Royal Academy of Engineering: Transforming Systems Through Partnership (China) under Grant TSPC1017. Recommended for publication by Associate Editor M. J. Scott. *(Corresponding author: Hong Li.)*

Wenzhe Su, Hong Li, Zuoxing Wang, and Xueyang Liu are with the School of Electrical Engineering, Beijing Jiaotong University, Beijing 100044, China (e-mail: wenzhesu@bjtu.edu.cn; hli@bjtu.edu.cn; zxwang2@bjtu.edu.cn; 21121444@bjtu.edu.cn).

Changlin Ji is with the Active Safety Technology–Steering Electronics Department from ZF Automotive Technologies Company, Ltd., Shanghai 430058, China (e-mail: changlin.ji@zf.com).

Baihua Zhang is with the Institute of Engineering Thermophysics, Chinese Academy of Sciences, Beijing 100045, China (e-mail: zhangbaihua@iet.cn).

Color versions of one or more figures in this article are available at https://doi.org/10.1109/TPEL.2023.3307572.

Digital Object Identifier 10.1109/TPEL.2023.3307572

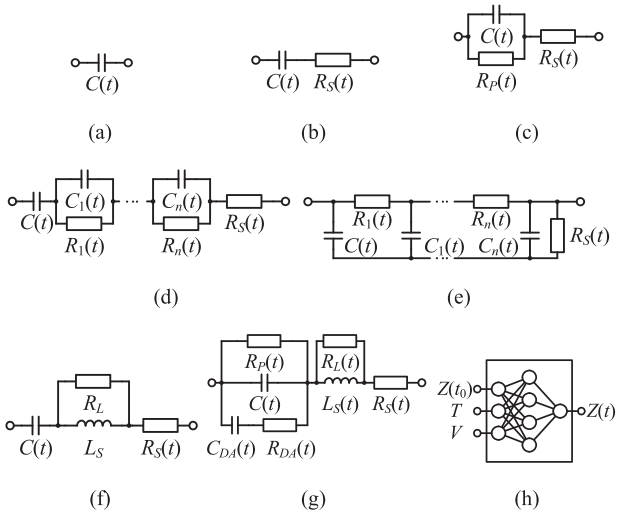

Fig. 1. Aging models of capacitors. (a) Ideal capacitor model. (b) RC series model. (c) RC series-parallel model. (d) Foster-type RC network model. (e) π-type RC network model. (f) RLC series parallel equivalent model. (g) Complicated RLC series parallel equivalent model. (h) Neural network-based model.

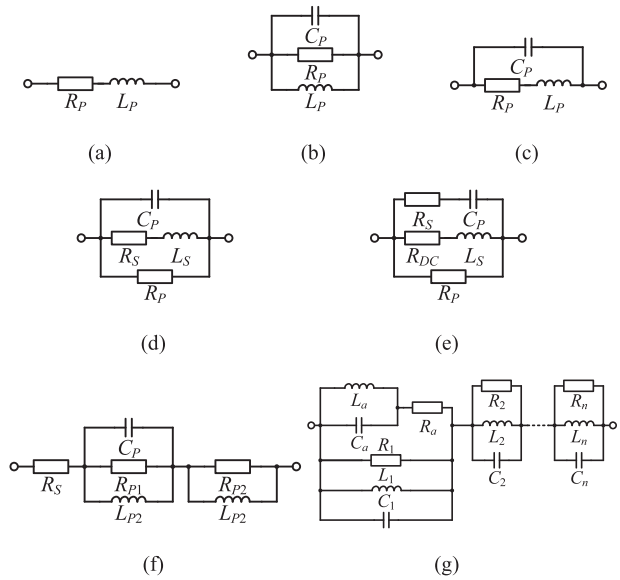

Fig. 2. Models of inductors. (a) RL series model. (b) RLC parallel model. (c)–(e) Different type RLC series-parallel model. (f) Complicated RLC series-parallel model. (g) Foster-type RC network models.

It can be concluded that the existing model has the following limitations: 1) The aging model focuses on a few frequency points, and the frequency is low, which is not suitable for EMI filter design. 2) The current model is essentially a black box model, which is only suitable for the description of external characteristics. Therefore, the parameters obtained by this type of model's parasitic parameter extraction method are multisolution, and it is difficult to be used to establish the capacitor aging model. 3) Although the existing literature accurately describes the high-frequency impedance characteristics of the inductor, the research on whether the high-frequency impedance characteristics of the inductor are affected by aging is blank. The limitations described in 1) and 2) will give detailed evidence in Section II problem description in this article.

EMI filter is the most critical part of EMI suppression, and its research is of representative significance. Aiming at the above-mentioned problems, this article proposes a lumped parameter high-frequency aging model based on electromagnetic field analysis. It is noted that this article is the extension and continuation of the research [22]. The innovations of this article are as follows: 1) The capacitor model based on electromagnetic field analysis is proposed in this article; the model considers the actual physical structure of passive devices and can describe the broadband characteristics of its EMC design. 2) Simultaneously, the parameters of the lumped model correspond to the physical meanings one by one. Based on the sectionalized frequency parameter-extracting (SFPE) method mentioned in this article, the uniqueness of the proposed model is guaranteed, and the aging law of the device can be described. 3) This article proposes a modeling method of high-frequency aging model based on a single high-frequency impedance measurement. The aging prediction of EMI filter performance can be completed using the existing datasheet and aging data set.

The rest of this article is organized as follows. Section II provides evidence of the limitations of the current research and introduces the problems addressed by the innovations of this article. Section III introduces the electromagnetic field analysis methods of passive devices such as capacitors and inductors and introduces the calculation method of the lumped parameter model. Section IV introduces the SFPE method. Section V introduces the effect of capacitor aging on various parameters and establishes a complete high-frequency aging model. Section VI predicts the change law of the EMI filter insertion loss performance affected by aging and the influence on the conducted EMI emission spectrum by means of simulation and experiment. Finally, Section VII concludes this article.

II. Problem Description

In this section, quantitative data are given as evidence to point out the limitations of the current model by reproducing the model and parameter extraction method in the current study. In view of the limitations of the current model, the research ideas of this article are further determined.

First, the RC network model in [12], as shown in Fig. 1(d), and the RLC series-parallel equivalent model in [14], as shown in Fig. 1(f), are reproduced and analyzed. The above-mentioned models are used to describe the impedance characteristics of the X-type capacitor, as shown in Fig. 3(a). It can be seen that the RC network model in [12] can accurately describe the impedance characteristics in the frequency range from 500 Hz to 95 kHz. The RLC equivalent model in [14] can describe the impedance characteristics in the range of 500 Hz to 900 kHz, and 2.4 MHz to 30 MHz. Through impedance analysis, the impedance in the frequency range from 500 Hz to 900 kHz determines the value of the model parameter C, and the impedance in the frequency range from 2.4 to 30 MHz determines the value of the model parameter L_S. At the same time, the parameters C and L_S determine the resonance point of the impedance. It

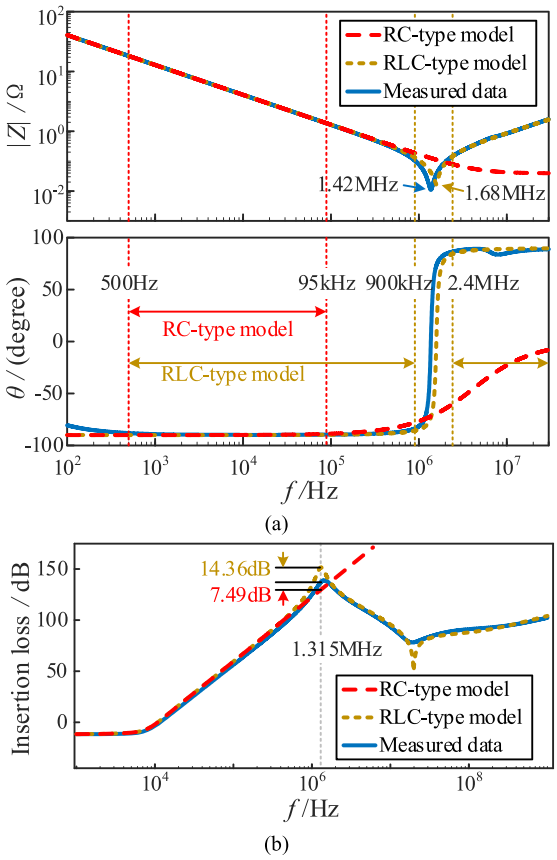

Fig. 3. Comparison of models. (a) Impedance-frequency characteristics described by RC network model [12] and complicated RLC series-parallel equivalent model in [14]. (b) π-type DM EMI filter insertion loss characteristics described by RC network model [12] and RLC series-parallel equivalent model in [14].

TABLE I
CONVERGENCE SOLUTION OBTAINED BY THE SAME EXTRACTION METHOD

Models	Values			
Fitting model I	R_P (kΩ)	C (μF)	C_{DA} (nF)	R_{DA} (MΩ)
	12.130	0.963	9.451	1.056
	R_L (MΩ)	L_S (nH)	R_S (mΩ)	
	1.431	13.555	0.102	
Fitting model II	R_P (MΩ)	C (μF)	C_{DA} (nF)	R_{DA} (kΩ)
	1.021	1.063	14.600	7.031
	R_L (kΩ)	L_S (nH)	R_S (mΩ)	
	11.201	12.565	0.098	

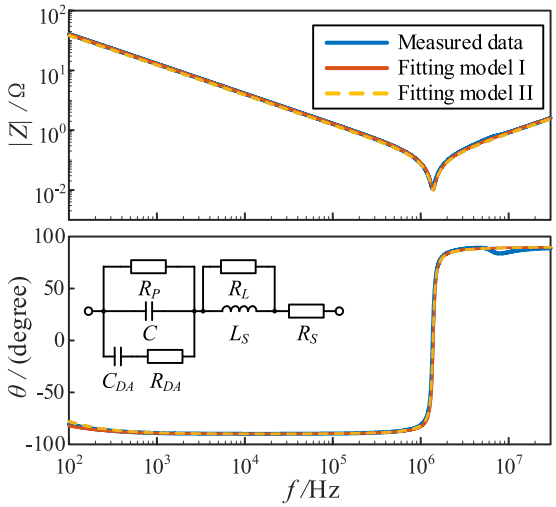

Fig. 4. Limitations of complicated RLC series-parallel equivalent model in [15].

can be seen that the model does not have enough degrees of freedom to describe the information of the resonance point, and the impedance fitting error at the resonance point is relatively large. The measured resonance point frequency is 1.42 MHz, while the fitted resonance point frequency is 1.68 MHz.

Further, use the compared model to calculate the insertion loss of the π-type DM EMI filter. Among them, the two X-type capacitors in the π-type DM EMI filter adopt the model to be compared, and the inductor adopts the measured data of the 500 nH DM inductor, the insertion loss calculation results are shown in Fig. 3(b).

For the RC network model, at the frequency of 1.315 MHz, the impedance phase angle is larger than the measured data, thus the calculated insertion loss is smaller than the measured insertion loss with an error of 7.49 dB. For the RLC equivalent capacitance model, the impedance phase angle at 1.315 MHz is smaller than the measured data, thus the calculated insertion loss is greater than the measured insertion loss with an error of 14.36 dB. According to engineering experience, the operating frequency of the DM EMI filter of the power electronic converter is 150 kHz to 2 MHz, and an error higher than 7.49 dB will have a significant impact on the design of the EMI filter.

Continue to discuss the complicated RLC equivalent circuit model in [14], as shown in Fig. 1(g). According to [14], the term R_S is the equivalent series resistance (ESR). The term R_P represents the leakage resistance of the dielectric. The terms L_S and R_L denote the parasitic inductance and resistance of the capacitor leads and terminals, respectively. The terms C_{DA} and R_{DA} are related to the polarization effect of dielectric materials. Although the parameters in the model correspond to the physical meaning of the electromagnetic field in the capacitor, the topology of the lumped elements of the model is obtained by inference, and the model is still a black box model in essence. Table I shows the convergence solution obtained by the same extraction method under two different initial values.

It can be seen that both convergence solutions can accurately describe the impedance characteristics of the component, as shown in Fig. 4. It is because the existing models are black-box models that can only describe the external characteristics of the model. The parasitic parameters are directly extracted from the parasitic parameters of the black box, and the obtained parameters are multisolution, which is challenging to be used to establish the capacitor aging model.

It can be seen that the direct application of the current model to EMI design has limitations. This article conducts research around the above-mentioned problems: first, it is necessary to

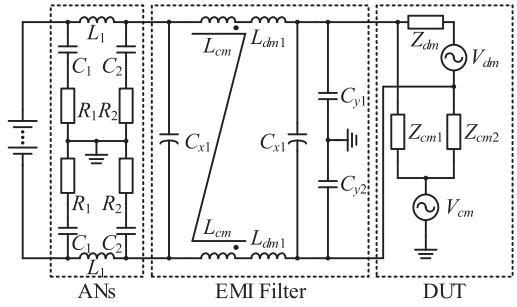

Fig. 5. Two-section EMI filter typical application in EVs.

propose a circuit model with sufficient accuracy, which needs to be guaranteed by the corresponding circuit topology; at the same time, this article needs to propose a parameter extraction method oriented to engineering practice and ensure that the extracted parameters are unique. This is the key to the model's applicability to aging prediction.

III. High-Frequency Model Establishment of Capacitors and Inductors

Unintuitive noise source waveforms can be decomposed into a series of harmonics so that the impedance of passive components at different frequencies can be tailored to keep EMI within standard limits. This requires an understanding of the frequency-dependent characteristics of the EMI propagation path impedance model. The high-frequency band range studied in this article is 150 kHz to 30 MHz, which is also a common frequency band for conducted EMI measurement.

The typical application in EVs of a two-section EMI filter is shown in Fig. 5. An EMI filter is designed to suppress the EMI emission of the DUT. It should be noted that there are no artificial networks (ANs) in practical EVs. ANs are used to simulate the typical impedance of sensitive equipment to measure the EMI emitted by DUT, in the EMI emission measurement based on the corresponding EMC standard [23]. This article focuses on the impedance of the capacitors and inductors themselves.

A. Capacitors

According to the function of capacitors, capacitors in EMI filters can be divided into X-type capacitors and Y-type capacitors. The X-type capacitor is connected between the positive power line and the negative power line, and the Y-type capacitor is connected between the power line and the ground. One model of an X-type capacitor and a Y-type capacitor are shown in Fig. 6.

First, establish the high-frequency model of the X-type capacitor. According to [24], the X-type capacitor is made by winding a plastic film sprayed with metal aluminum under the vacuum environment, and its structure is shown in Fig. 7. Among them, the term d_1 represents the thickness of the metalized coating, the term d_2 represents the thickness of the plastic film, the terms h_1 and l_1 represent the length and width of the plane of the winding center, and the term N represents the total number of winding

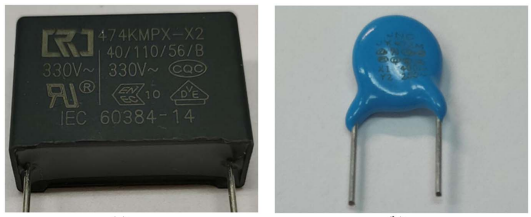

Fig. 6. Capacitors in EMI filter. (a) X-type capacitor. (b) Y-type capacitor.

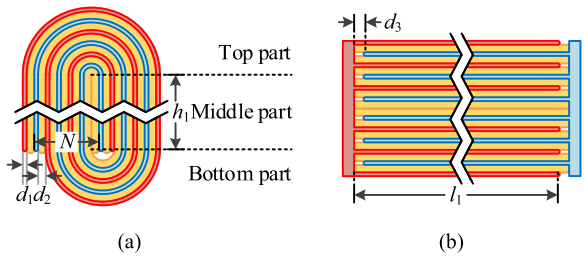

Fig. 7. Structure of X-type capacitor. (a) Side sectional view. (b) Top sectional view.

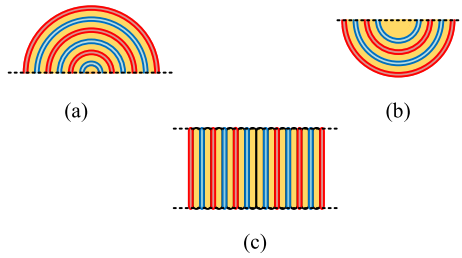

Fig. 8. Three parts of X-type capacitor for electromagnetic field analysis. (a) Top part. (b) Bottom part. (c) Middle part.

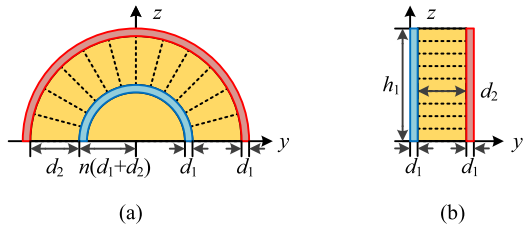

Fig. 9. Electromagnetic field analysis of capacitance. (a) Top part and bottom part. (b) Middle part.

layers. According to [25], the thickness of d_1 is 0.01–0.1 μm, and the thickness of d_2 is 10–1 μm.

According to the side view, the electromagnetic field inside the capacitor will be solved in three parts, as shown in Fig. 8. The geometric structure of the top and bottom of the capacitor is a concentric circle structure. According to [26], the electromagnetic field distribution is shown in Fig. 9(a), and the dotted line in the figure indicates the electric force line. The electromagnetic field distribution of this structure satisfies the Laplace equation, which can be solved to obtain the electromagnetic field of this area where the electric field is concentrated on the top and bottom

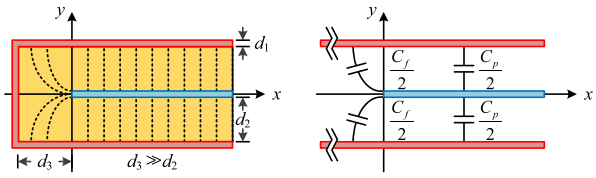

Fig. 10. Electromagnetic field analysis of plate capacitance considering fringe capacitance. (a) Electromagnetic field analysis. (b) Equivalent circuit.

of the capacitor, and the capacitance C_{uc} and C_{dc} can be used to describe the characteristics of this area. The terms C_{uc} and C_{dc} are shown as follows:

$$C_{uc}(n) = \frac{\pi \varepsilon l_1}{\ln\left(1 + \frac{d_2}{n(d_1+d_2)}\right)} \quad (n = 1, \cdots, N-1) \tag{1}$$

$$C_{dc}(n) = \frac{\pi \varepsilon l_1}{\ln\left(1 + \frac{d_2}{n(d_1+d_2)}\right)} \quad (n = 2, \cdots, N) \tag{2}$$

where the term n is the location of winding layers. The term ε the dielectric constant. According to [27], the dielectric constant of the plastic film is subjected to aging, and the impedance - frequency is approximately constant.

The geometric structure in the middle of the capacitor is a plate structure. According to [26], its electromagnetic field distribution is shown in Fig. 9(b). Similarly, the electromagnetic field distribution of the plate structure satisfies the Laplace equation, and the term C_p is used to describe the characteristics of this region, shown as follows:

$$C_p = 2(N-1)\frac{\varepsilon h_1 l_1}{d_2}. \tag{3}$$

As shown in the cross-section of the capacitor in Fig. 7(b), the capacitor plates are connected by the metal on both sides of the capacitor, and according to [28], d_3 is usually larger than 0.5 mm. Its electromagnetic field distribution is shown in Fig. 10(a). Since d_3 is much larger than d_2, it can be considered that the red plate extends wirelessly toward the negative direction of x-axis, as shown in Fig. 10(b). According to [26], the capacitance per unit length due to edge effects is shown in the following equations:

$$c_f = \frac{\varepsilon}{\pi}\left\{\frac{4}{r}\ln\left(\frac{1}{r}+1\right) - \left(\frac{1}{r}-1\right)\ln\left(\frac{1}{r^2}-1\right)\right\}(F/m) \tag{4}$$

$$r = 1 - \frac{d_1}{2d_2}. \tag{5}$$

The edge effect capacitance can be obtained as follows:

$$C_f = \frac{\varepsilon}{\pi}\left\{\frac{4}{r}\ln\left(\frac{1}{r}+1\right) - \left(\frac{1}{r}-1\right)\ln\left(\frac{1}{r^2}-1\right)\right\}L \tag{6}$$

where the term L is the length of plastic film sprayed with metal aluminum.

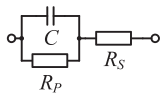

Fig. 11. Lumped parameter model corresponding to the electromagnetic field between capacitor plates.

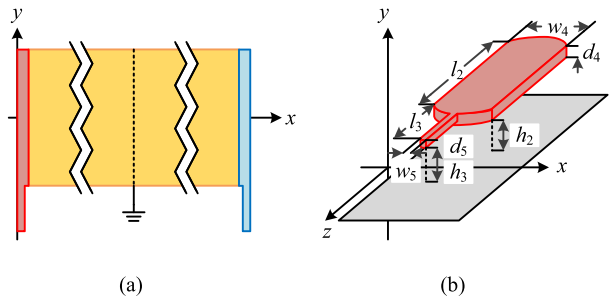

Fig. 12. Electromagnetic field analysis of capacitor pins. (a) Structure of the capacitor pins. (b) Geometric parameters of the capacitor pins.

The capacitance of this structure can be obtained as follows:

$$C = C_p + C_f + \sum_{n}^{N}\left[C_{uc}(n) + C_{dc}(n)\right]. \tag{7}$$

Since the capacitor dielectric is in the high-frequency electromagnetic field, the electrode turns lossy can be described by the dielectric loss angle, and the corresponding lumped parameter model is the equivalent series resistance R_S, as shown in the following equation:

$$R_S = X_C \tan\sigma = \frac{\tan\sigma}{\omega C}. \tag{8}$$

Capacitor dielectric has a certain conductivity, this feature also causes current to pass through the capacitor under dc, and this resistance corresponds to R_P, dc leakage resistance, as shown in the following equation:

$$R_P = \frac{\rho d_2}{S(l_1, N)}. \tag{9}$$

The lumped parameter model corresponding to the electromagnetic field between the capacitor plates is shown in Fig. 11.

The metal coating of the capacitor is connected through two side electrodes, as shown in Fig. 12. According to the superposition theorem of electromagnetic field, the electromagnetic field of the side electrodes is analyzed. According to [29], the symmetrical structure can be regarded as the transmission line model of the plate-to-capacitor symmetry plane, and the electrodes on the side of the capacitor can be regarded as the connection of the two transmission lines l_2 and l_3. Through the extraction of the capacitance of the 3-D structure [30], the capacitance C_1 of the l_2 segment is shown as follows:

$$C_1 = l_2\varepsilon\left\{1.15\left(\frac{w_4}{h_2}\right) + 2.80\left(\frac{d_4}{h_2}\right)^{0.222}\right\} \times 10^2. \tag{10}$$

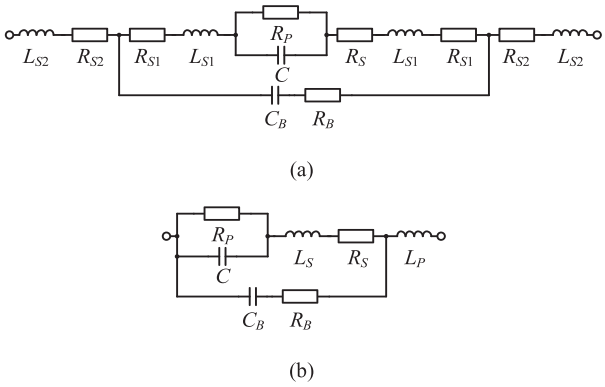

Fig. 13. X-type capacitor high-frequency equivalent model. (a) Lumped parameter model. (b) Simplified lumped parameter model.

The capacitance C_2 of the l_3 segment is shown as follows:

$$C_2 = l_3\varepsilon\left\{1.15\left(\frac{w_5}{h_3}\right)+2.80\left(\frac{d_5}{h_3}\right)^{0.222}\right\}\times 10^2. \quad (11)$$

In a transmission line, the inductance can usually be obtained according to the unified relationship between electric field and magnetic field [26], shown as follows:

$$L_1 = \frac{\varepsilon}{c^2 C_1}. \quad (12)$$

Using the T-type equivalent circuit model of the transmission line, the lumped parameter model of the pin is finally obtained, as shown in Fig. 13(a), which is finally simplified to Fig. 13(b).

The common structure of the Y-type capacitor consists of a metalized plate, a ceramic dielectric, and metal pins. Its capacitor structure is a circular flat capacitor. The parameter C in the high-frequency aging model can be replaced by using the following equation:

$$C = \frac{\varepsilon A}{d} \quad (13)$$

where ε is the dielectric constant, A is the surface area of the capacitor, and d is the thickness of the capacitor. Thus, the Y-type capacitor model can also use the same model as shown in Fig. 13.

B. Inductors

The inductors in the EMI filter can be divided into DM inductors and CM inductors according to their functions. The structures of commonly used DM inductors and CM inductors are shown in Fig. 14.

The CM inductor structure is different from the DM inductor structure, but the topological composition of the CM inductor model is usually common to the DM inductor model. The specific principles are explained as follows:

The commonly used DM inductor model in the industry is shown in Fig. 15(a). Among them, C_{K1} represents the parasitic capacitance of the winding to the ground. CK_1 is usually directly related to the grounding of the PCB, so it is usually not included in the inductor model. The circuit model composed of R_{P1}, C_{P1}, and L_1 is generally considered to be the model of the inductor itself. As mentioned in the introduction, this part of this circuit topology can be a variety of structures. Here, the parallel connection of R_{P1}, C_{P1}, and L_1 will be used for further analysis, where R_{P1} represents the core loss when the high-frequency current passes through the inductor; C_{P1} represents the interturn parasitic capacitance during winding, and L_1 represents the inductance formed by the winding around the core.

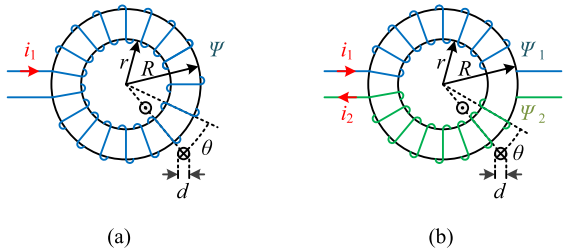

Fig. 14. Structure of inductors in EMI filter. (a) DM inductors. (b) CM inductors.

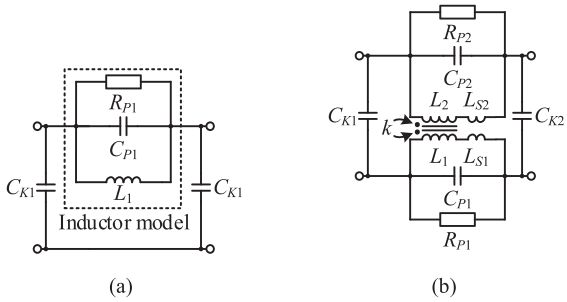

Fig. 15. Model of inductors in EMI filter. (a) DM inductors. (b) CM inductors.

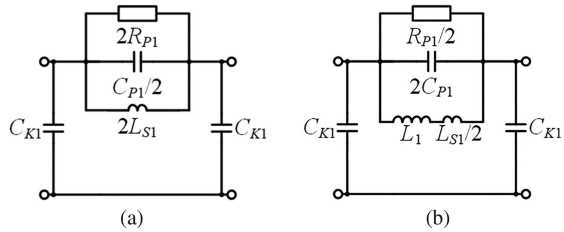

Fig. 16. DM and CM model decomposition of CM inductor. (a) DM impedance model. (b) CM impedance model.

The winding of the CM inductor is similar to that of the DM inductor in Fig. 14(b), and the corresponding model of the CM inductor is shown in Fig. 15(b). Unlike the DM inductor model, the CM inductor model includes a mutual inductance model. The term k is coupling coefficient, and the term L_1 and L_2 are coupling inductance. The terms RP_1, CP_1, RP_1, and $CP1$ have the same definition as DM inductor. While CK_1 represents the sum of the parasitic inductance between the windings and the parasitic inductance between the windings to the ground.

When the CM inductor adopts the mirror winding method, $C_{K1} = C_{K2}, R_{P1} = R_{P2}, C_{P1} = C_{P2}, L_1 = L_2$. At this time, the CM inductor can be decomposed into a CM impedance model of the CM inductor and a DM impedance model of the CM inductor, as shown in Fig. 16. It can be seen that the CM impedance model

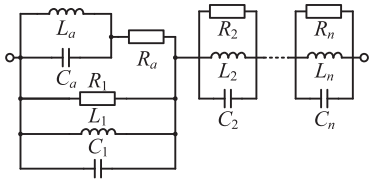

Fig. 17. Equivalent circuit model of inductor.

of the CM inductor and the DM impedance model of the CM inductor have the same circuit topology as the DM inductor.

The Foster inductor model can describe the impedance-frequency characteristics of inductors in a wide frequency range [31]. This model will be used as the high-frequency model of DM inductors and CM inductors in this article, as shown in Fig. 17.

IV. Sectionalized Frequency Parameters Extracting Method

Based on the above-mentioned content, the topology and parameter calculation method of the discrete capacitor and inductor lumped parameter model in the passive filter are determined through electromagnetic field analysis. Although the topology of the model is determined, in the actual application of the model, the values of the above-mentioned parameters are not easy to obtain, and there is an error with the actual measurement. It is necessary to use the parameter extraction method based on the actual measurement to correct the model parameters.

According to Fig. 13(b), the impedance of simplified equivalent circuit model can be obtained as shown in the following equations:

$$Z = \frac{\left(R_B\sigma_2 + \frac{\sigma_1}{C_B\omega}\right)\sigma_5 - \left(R_B\sigma_1 - \frac{\sigma_2}{C_B\omega}\right)\sigma_4}{\sigma_3} + \mathrm{j}\left[\frac{\left(R_B\sigma_1 - \frac{\sigma_2}{C_B\omega}\right)\sigma_5 + \left(R_B\sigma_2 + \frac{\sigma_1}{C_B\omega}\right)\sigma_4}{\sigma_3} + \omega L_P\right] \tag{14}$$

$$\begin{cases} \sigma_1 = L_S\omega - \frac{R_{P1}^2}{C\omega\left(R_{P1}^2 + \frac{1}{C^2\omega^2}\right)} \\ \sigma_2 = R_S + \frac{R_{P1}}{C^2\omega^2\left(R_{P1}^2 + \frac{1}{C^2\omega^2}\right)} \\ \sigma_3 = \sigma_4^2 + \sigma_5^2 \\ \sigma_4 = \frac{1}{C_B\omega} - L_S\omega + \frac{R_{P1}^2}{C\omega\left(R_{P1}^2 + \frac{1}{C^2\omega^2}\right)} \\ \sigma_5 = R_B + R_S + \frac{R_{P1}}{C^2\omega^2\left(R_{P1}^2 + \frac{1}{C^2\omega^2}\right)} \end{cases}. \tag{15}$$

Let the resistance values R_S and R_B be zero, while the resistance values R_P be infinite, as shown in Fig. 18, and draw its impedance characteristic curve, as shown in Fig. 19. It can be obtained that the characteristic impedance has the following characteristics: 1) The imaginary part of the impedance has three zero points. Among them, resonance points A and C are the series resonance points, while resonance point B is the parallel resonance point. 2) The impedance characteristic of the zero-resistance equivalent model is divided into four areas by three

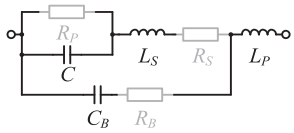

Fig. 18. None-resistance high-frequency equivalent model.

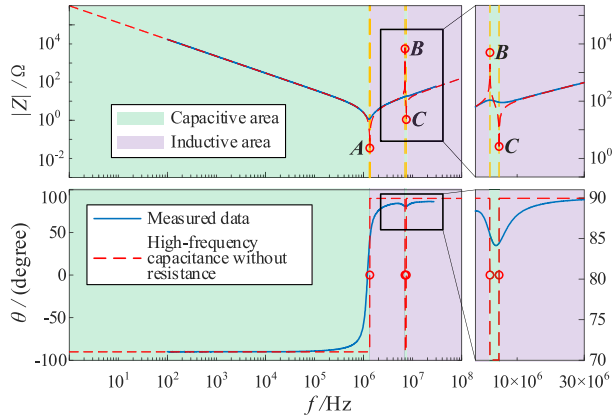

Fig. 19. Impedance characteristic of zero resistance high-frequency equivalent model.

zero points. The area where the phase is $-90°$ is the capacitive area. The area where the phase is $90°$ is the inductive area. 3) The magnitude characteristic in the impedance characteristic curve contains a minimum point at frequency point A, while the phase characteristic in the impedance characteristic curve contains a minimum point between the resonance point B and the resonance point C. The frequencies of the three resonance points can be obtained as follows:

$$f_A = \sqrt{\frac{b - \sqrt{b^2 - 4a}}{2a}} \tag{16}$$

$$f_B = \frac{1}{2\pi}\sqrt{\frac{1}{L_S}\left(\frac{1}{C} + \frac{1}{C_B}\right)} \tag{17}$$

$$f_C = \sqrt{\frac{b + \sqrt{b^2 - 4a}}{2a}} \tag{18}$$

where

$$\begin{cases} a = L_P L_S C C_B \\ b = L_S C + L_P C_B + L_P C \end{cases}. \tag{19}$$

When C is much larger than C_B, (16) can be simplified to (20).

$$f_A = \frac{1}{2\pi\sqrt{L_{\text{sum}} C_{\text{sum}}}} \tag{20}$$

where

$$\begin{cases} \frac{1}{C_{\text{sum}}} = \frac{1}{C} + \frac{1}{C_B} \\ L_{\text{sum}} = L_S + L_P \end{cases}. \tag{21}$$

The influence of each parameter on the impedance characteristic curve is described in detail in the Appendix. The following

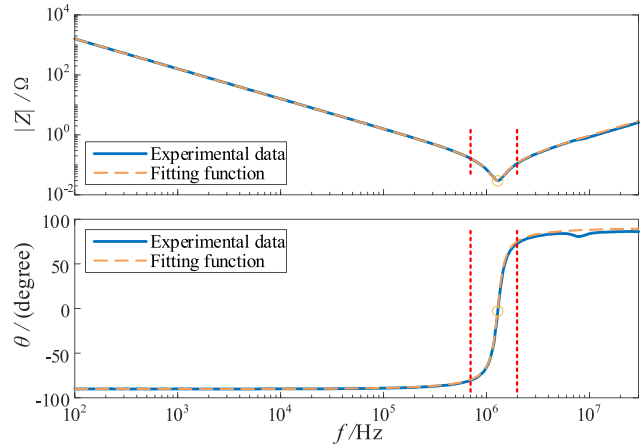

Fig. 20. Frequency area selected in step 1 of the SFPE extraction method.

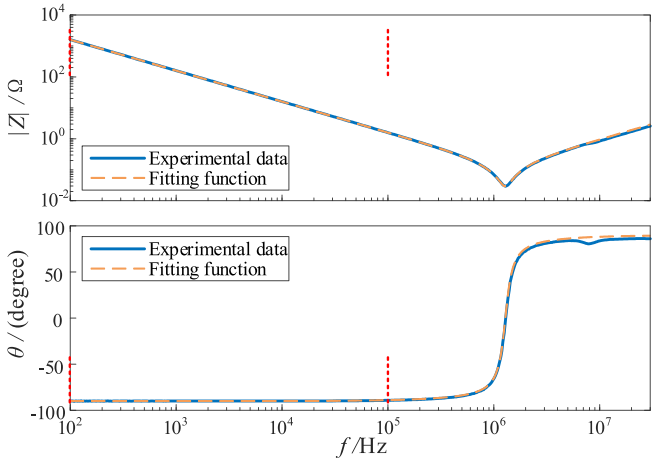

Fig. 21. Frequency area selected in step 2 of the SFPE extraction method.

conclusions can be drawn: 1) C, R_P, and R_S determine the impedance characteristics of frequencies smaller than point A. 2) L_S, C_B, R_B, and L_P determine the characteristics of frequencies greater than point A. Therefore, the parameter value can be extracted based on the frequency band. The following sectionalized frequency parameter extraction method is proposed based on the above-mentioned analysis.

1) Term C_{sum} L_{sum} R_{sum} *Extraction:* Based on (14) and the primary circuit principle, in the 700 kHz–2 MHz frequency band, shown in Fig. 20, (13) is approximated as follows:

$$Z = R_S + \mathrm{j}\omega L_{\mathrm{sum}} + \frac{1}{\mathrm{j}\omega C_{\mathrm{sum}}}. \tag{22}$$

The complex function can be split into a real part function and an imaginary part function for fitting as follows:

$$\begin{cases} func.1 = \mathrm{real}\,(Z) = R_S \\ func.2 = \mathrm{imag}(Z) = \omega L_{sum} - \frac{1}{\omega C_{sum}} \end{cases}. \tag{23}$$

2) Term R_P *Extraction:* In the 100 Hz–100 kHz frequency band, shown in Fig. 21, (14) is approximated as follows:

$$Z = \frac{1}{R_P + \frac{1}{\mathrm{j}\omega C_{\mathrm{sum}}}} + \mathrm{j}\omega L_{\mathrm{sum}} + R_{\mathrm{sum}}. \tag{24}$$

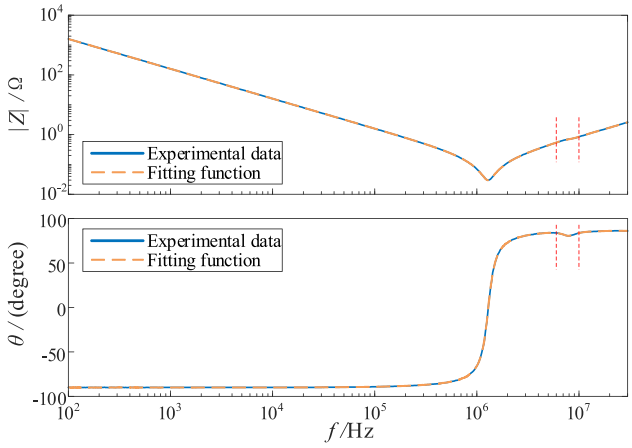

Fig. 22. Frequency area selected in step 3 of the SFPE extraction method.

While the fitting function is as follows:

$$\begin{cases} func.3 = \mathrm{real}\,(Z) = \omega L_{\mathrm{sum}} - \dfrac{R_P^2}{\omega C_{\mathrm{sum}}\left(R_P^2 + \frac{1}{\omega^2 C_{\mathrm{sum}}^2}\right)} \\ func.4 = \mathrm{imag}(Z) = R_{\mathrm{sum}} + \dfrac{R_P}{\omega^2 C_{\mathrm{sum}}^2\left(R_P^2 + \frac{1}{\omega^2 C_{\mathrm{sum}}^2}\right)} \end{cases}. \tag{25}$$

3) Term C_B L_P R_S R_B *Extraction:* In the 6–10 MHz frequency band, shown in Fig. 22, (13) and (14) are determined by all parameters. Thus, the fitting function is as follows:

$$\begin{cases} func.5 = \mathrm{real}\,(Z) = \dfrac{\left(R_B\sigma_2 + \frac{\sigma_1}{C_B\omega}\right)\sigma_5 - \left(R_B\sigma_1 - \frac{\sigma_2}{C_B\omega}\right)\sigma_4}{\sigma_3} \\ func.6 = \mathrm{imag}\,(Z) = \dfrac{\left(R_B\sigma_1 - \frac{\sigma_2}{C_B\omega}\right)\sigma_5 + \left(R_B\sigma_2 + \frac{\sigma_1}{C_B\omega}\right)\sigma_4}{\sigma_3} \end{cases}. \tag{26}$$

V. High-Frequency Aging Model Establishment of Capacitors and Inductances

In this article, the accelerated aging experiments of electrical and environmental stress are carried out on various commonly used square-shaped X-type capacitors, pie-shaped Y-type capacitors, DM inductors, and CM inductors, as shown in Fig. 23.

The electrical stress aging test platform fixtures for capacitors and inductors are designed, respectively, as shown in Fig. 24. Among them, the capacitor applies 1.2 times the rated voltage as a constant electrical stress, and the inductor applies 1.5 times the rated current as a constant electrical stress.

The electrical stress and environmental stress aging experiment platform is shown in Fig. 24. Accelerated aging experiments were performed on capacitors and inductors under constant thermal stress (135 °C) and constant humidity (50%). In order to apply 1.5 times of the rated current to the inductor as a constant electrical stress, it is necessary to use a series resistance for the inductor as a bias load outside the environmental chamber.

A. Capacitors

According to the concept of capacitor life and its reliability, after the capacitor fails, its impedance-frequency characteristic aging no longer satisfies the Arrhenius model [32]. It is necessary

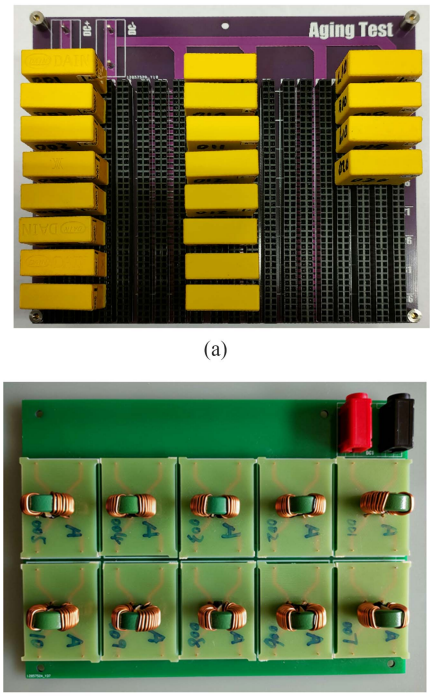

Fig. 23. Electrical stress accelerated aging test fixture. (a) X-type capacitors and Y-type capacitors test fixture. (b) DM inductor and CM inductor test fixture.

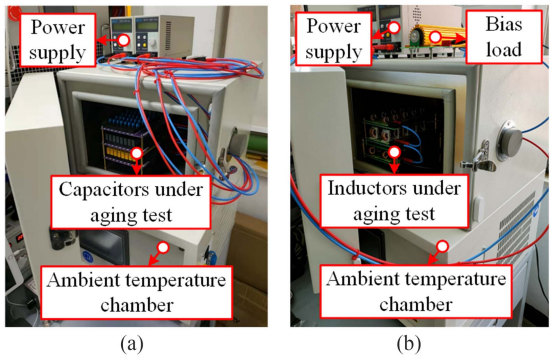

Fig. 24. Environmental stress accelerated aging test fixture. (a) X-type and Y-type capacitors test setup. (b) DM inductor and CM inductor test setup.

to perform device failure judgment and frequency impedance tests on capacitors and inductors at intervals of aging time. The measurement method is shown in Fig. 25. Use a low-frequency capacitive impedance analyzer to measure the capacitance value and the dielectric loss tangent, and its variation with time is shown in Fig. 26. According to the datasheet provided by the capacitor device, capacitors can be judged whether they are invalid by the value of electrical parameters: (1) The capacitance value under the 1 kHz measurement drops below 90%. (2) The dielectric loss tangent increases to specific value or more under the 1 kHz measurement. It can be seen that the capacitor fails after the accelerated aging test is carried out for 600 h. Therefore, this article does not consider the data after capacitor failure.

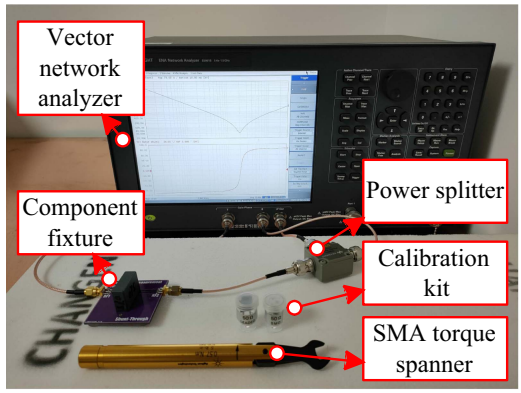

Fig. 25. Component impedance test.

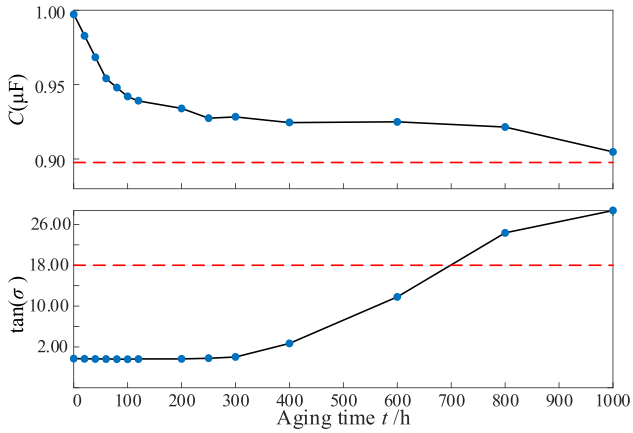

Fig. 26. Variation with aging time of capacitance value and the dielectric loss tangent of X-type Capacitance.

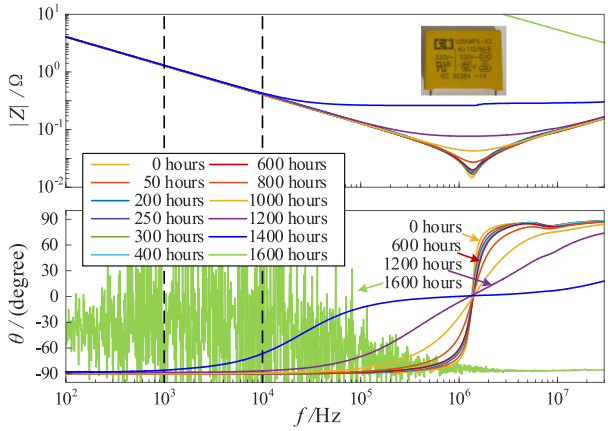

Fig. 27. X-type Capacitance impedance characteristics change with time.

Use a vector network analyzer to measure the impedance of the capacitor, shown in Fig. 27. According to [24], the structure of the capacitor may change after failure, and its aging model will no longer satisfy the Arrhenius model, so the data after 600 h will no longer be used.

Based on the experimental data of the impedance characteristics of the accelerated aging experiment, using the SFPE

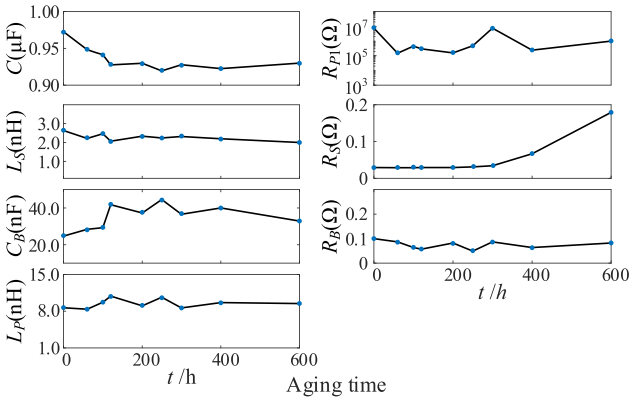

Fig. 28. Variations of each parameter of the high-frequency model with accelerated aging time.

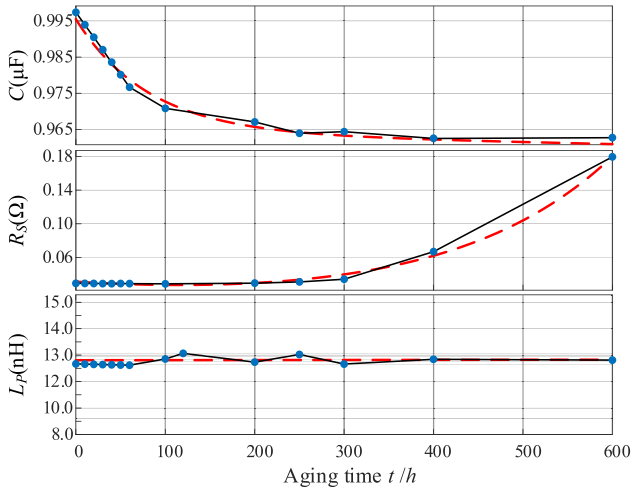

Fig. 29. Exponential fitting analysis of typical parameter.

TABLE II
EXPONENTIAL FUNCTION FITTING RESULTS

Parameters	a_0	b_0	c_0	d_0
C (F)	3.13×10^{-8}	-1.24×10^{-2}	9.64×10^{-7}	-5.55×10^{-6}
R_P (Ω)	7.06×10^{6}	-4.06×10^{-2}	8.55×10^{5}	1.33×10^{-3}
L_S (H)	1.57×10^{-10}	-3.91×10^{-3}	2.25×10^{-9}	-1.71×10^{-4}
R_S (Ω)	0.03×10^{-2}	-3.98×10^{-3}	5.86×10^{-3}	5.69×10^{-3}
C_B (F)	2.31×10^{-8}	-1.37×10^{-4}	3.39×10^{-11}	1.32×10^{-2}
R_B (Ω)	9.88×10^{-2}	-9.22×10^{-4}	5.73×10^{-3}	3.71×10^{-3}
L_P (H)	-1.08×10^{-12}	1.21×10^{-2}	1.27×10^{-8}	1.03×10^{-4}

TABLE III
EXPONENTIAL GOODNESS-OF-FIT ANALYSIS FOR EACH PARAMETER

Parameters	R^2	Adjusted R^2	RMSE
C	0.9792	0.9689	1.841×10^{-9}
R_P	0.2655	0.1737	$2.729\times10^{+6}$
L_S	0.2771	−0.0843	2.068×10^{-10}
R_S	0.9962	0.9943	3.570×10^{-3}
C_B	0.0598	−0.0576	6.896×10^{-8}
R_B	0.0021	−0.1226	1.852×10^{-2}
L_P	0.0077	−0.1164	3.156×10^{-10}

method based on Section III, the variations of each parameter of the high-frequency model changing with time are obtained, as shown in Fig. 28.

It can be seen intuitively that the parameters C and R_S may age in an exponential function. Finds an exponential fit to data with individual parameters over time. Take three typical parameters C, R_S, and L_P as examples for analysis.

Use the following fitting formula (27) to fit each parameter, and the fitting results are shown in Table II:

$$func.7 = a_0 e^{b_0 t} + c_0 e^{d_0 t}. \tag{27}$$

The goodness of fit can be quantitatively in Table III. The term SST is called the sum of squares about the mean, SSR is the sum of squares of the regression, SSE is the sum of squares due to error, and R^2 is R-square. While the residual degree of freedom v is defined as the number of response values n minus the number of fitted coefficients m estimated from the response values. MSE is the mean square error or the residual mean square, while RMSE is the root mean squared error [33].

According to [33], the adjusted R^2 statistic can take on any value less than or equal to 1, with a value closer to 1 indicating a better fit. Negative values can occur when the model contains terms that do not help to predict the response. An RMSE value closer to 0 indicates a fit more useful for prediction.

Based on the aging law reflected in Fig. 26, it is assumed that C and R_S are exponentially distributed. According to the above-mentioned mathematical basis, it can be seen from Table III that the aging laws of C and R_S are determined to satisfy the exponential function aging law (26). According to the L_P aging law in Fig. 29, it can be assumed that the data of L_P presents a normal distribution, and the Anderson–Darling (AD) test is used to test whether this assumption is correct. AD test results are shown in Table IV. It can be seen that the above-mentioned hypothesis cannot be rejected when the significance level α is 0.05, so it can be finally determined that the parameters R_P, L_S, C_B, R_B, and L_P are constant within the life of the capacitor.

Finally, the high-frequency aging model of X-type capacitor is shown in Fig. 30. According to the aging data of 20 capacitors in Fig. 31, the high-frequency aging model can be obtained based on the method proposed in this article. When the significance $a = 0.05$, the model is shown in Table V.

The meaning of the confidence interval in the figure is that the actual model has a 95% probability of being located in this interval, while the prediction interval means that the measured data has a 95% probability of being located in this interval.

TABLE IV
ANDERSON–DARLING TEST RESULTS FOR EACH PARAMETER

Parameters	Mean	Standard deviation	Anderson–Darling test
R_P (Ω)	2.16×10^{6}	2.90×10^{6}	Ture
L_S (H)	2.38×10^{-9}	2.64×10^{-10}	Ture
C_B (F)	2.34×10^{-8}	2.57×10^{-8}	Ture
R_B (Ω)	9.9×10^{-2}	7.20×10^{-3}	Ture
L_P (H)	1.28×10^{-8}	3.25×10^{-10}	Ture

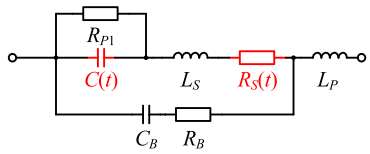

Fig. 30. High-frequency aging model of X-type capacitor.

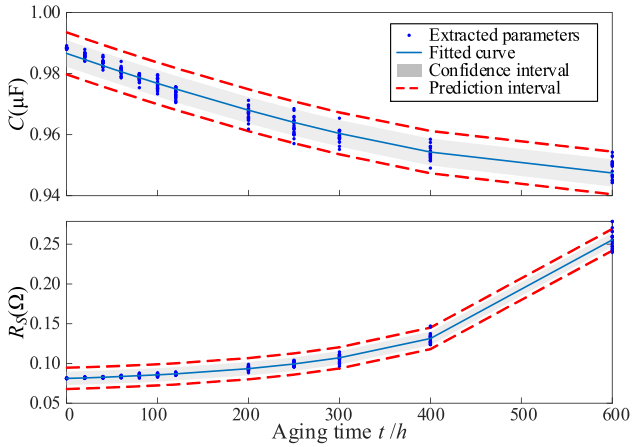

Fig. 31. Aging model of parameter C and R_S.

TABLE V
HIGH-FREQUENCY AGING MODEL OF X-TYPE CAPACITORS

Parameter		Mean	Min	Max
C (F)	a_0	9.70×10^{-7}	9.09×10^{-7}	1.03×10^{-6}
	b_0	-1.41×10^{-4}	-2.37×10^{-4}	-0.45×10^{-4}
	c_0	1.68×10^{-8}	-4.41×10^{-8}	7.77×10^{-8}
	d_0	2.01×10^{-3}	-8.68×10^{-4}	4.90×10^{-3}
R_S (Ω)	a_0	2.65×10^{-2}	2.65×10^{-2}	2.65×10^{-2}
	b_0	1.99×10^{-4}	1.99×10^{-4}	1.99×10^{-4}
	c_0	4.77×10^{-3}	4.77×10^{-3}	4.77×10^{-3}
	d_0	6.01×10^{-3}	6.01×10^{-3}	6.01×10^{-3}
R_P (MΩ)		2.15	3.13	4.00
L_S (nH)		2.37	2.21	2.54
C_B (nF)		24.66	21.72	24.99
R_B (mΩ)		98.22	94.51	103.71
L_P (nH)		12.89	12.59	13.00

It can be seen from Fig. 31 that the high-frequency aging model proposed in this article is representative.

Using the same analysis method, and it can be known that Y-type capacitors can also use the same topology of model. First, measure the Y-type capacitor impedance-frequency change law with aging, as shown in Table VI and Fig. 32.

It can be seen that the high-frequency aging model and parameter aging law of the Y-type capacitor are the same as those of the X-type capacitor, as shown in Fig. 33.

TABLE VI
HIGH-FREQUENCY AGING MODEL OF Y-TYPE CAPACITORS

Parameter		Mean	Min	Max
C (nF)	a_0	0.3936	0.2681	0.5190
	b_0	−0.0187	−0.0356	0.0019
	c_0	4.530	4.419	4.642
	d_0	-8.65×10^{-5}	-14.32×10^{-5}	-2.985×10^{-5}
R_S (mΩ)	a_0	140.5	−20.23	301.2
	b_0	1.24×10^{-4}	-5.681×10^{-3}	5.931×10^{-3}
	c_0	5.505	−166.3	177.3
	d_0	0.004389	−0.3263	0.0414
R_P (MΩ)		2.15	3.13	4.00
L_S (nH)		2.37	2.21	2.54
C_B (pF)		24.66	21.72	24.99
R_B (mΩ)		98.22	94.51	103.71
L_P (nH)		12.89	12.59	13.00

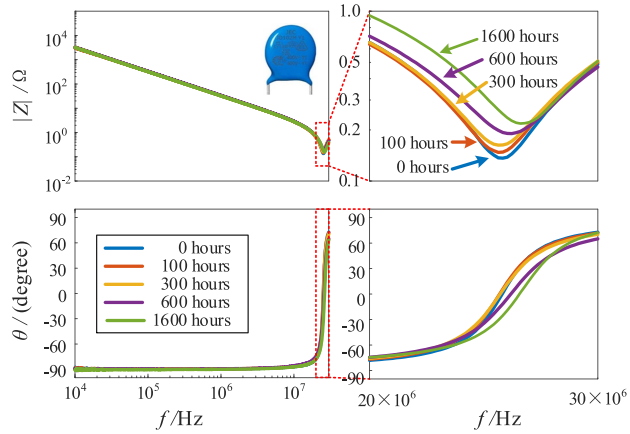

Fig. 32. Y-type capacitor impedance characteristics change with time.

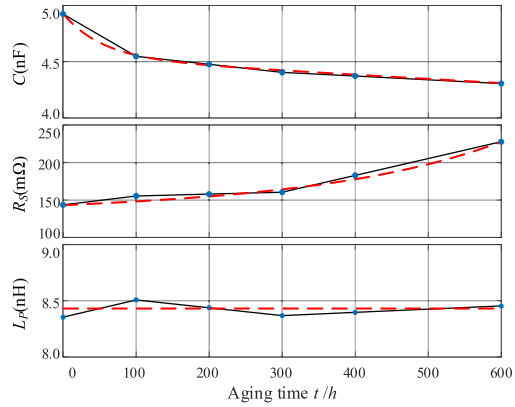

Fig. 33. Parameters change of the Y-type capacitor.

B. Inductors

Under the aforementioned environmental stress and electrical stress, the aging law of the CM inductor is shown in Fig. 34, while DM inductor is shown in Fig. 35. It can be seen that the aging caused by the thermal stress and electrical stress of the inductor is weak. The final high-frequency aging model is consistent with

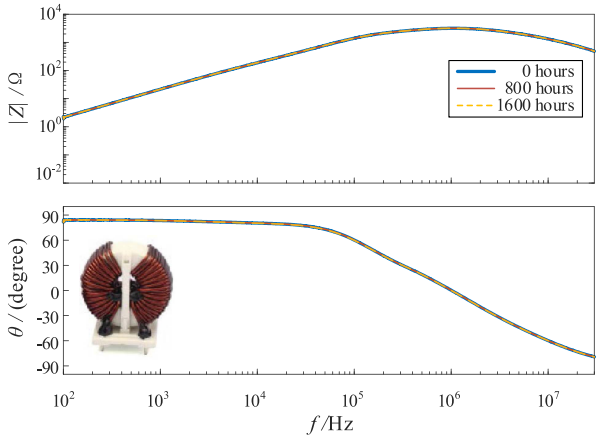

(a)

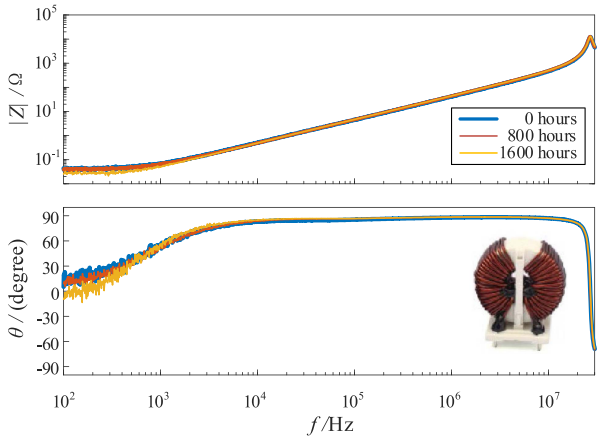

(b)

Fig. 34. Aging law of impedance characteristics of CM inductors. (a) DM component measurement. (b) CM component measurement.

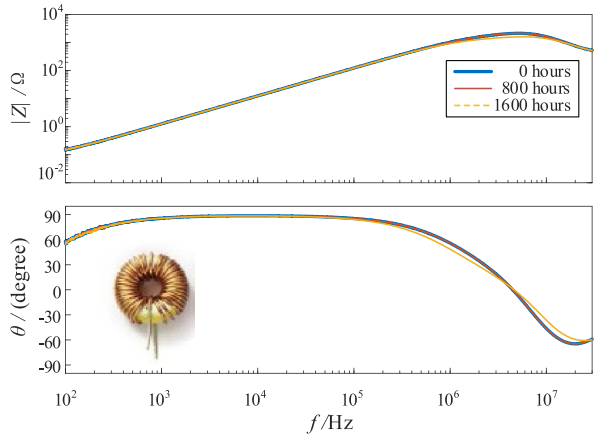

Fig. 35. Aging law of impedance characteristics of DM inductors.

the model in [31]. Each parameter in the model is constant, and its model can be extracted by using the method of measuring the mean.

Finally, this article determines the high-frequency aging model of capacitors and inductors under constant thermal stress and thermal stress. This method can establish an aging model

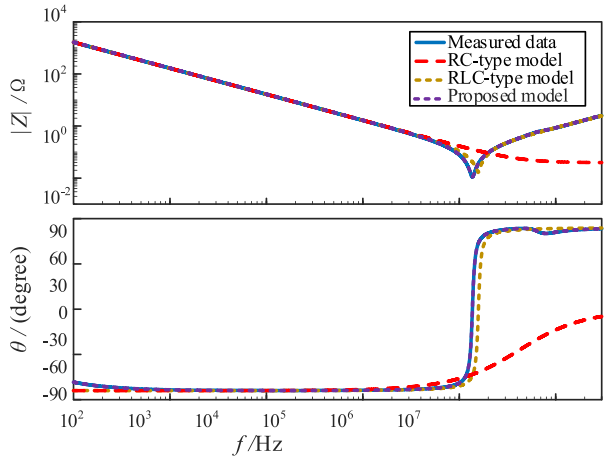

Fig. 36. Comparison of individual X-type capacitor impedance characteristics.

TABLE VII
PERFORMANCE FITTING COMPARISON OF DIFFERENT HIGH-FREQUENCY MODELS

Model	Items	Adjusted R^2	RMSE
RC-type model	Magnitude	0.7341	71.7635
	Argument	0.2793	2.48×10^3
RLC-type model	Magnitude	0.9178	55.7618
	Argument	0.7994	63.7739
Proposed model	Magnitude	0.9979	31.9318
	Argument	0.9955	78.9258

under the condition that the structures of the X-type capacitor and the Y-type capacitor are known.

VI. Experimental Verification of Practical Application

In this article, the following experiments are carried out to verify the model and the prediction ability of the high-frequency aging model: (1) The impedance fitting error of a single component. (2) Prediction of a single component impedance affected by aging. (3) Prediction of EMI spectrum by EMI filter affected by aging.

A. Impedance Fitting Error of a Single Component

First, the fitting performance of the high-frequency model to a single device is discussed. Compare the RC model, the RLC model, shown in Fig. 1, and the high-frequency model proposed in this article, as shown in Fig. 36 and Table VII.

It can be seen that among all the compared models, the high-frequency aging model proposed in this article has the highest adjusted R-square and the smallest RMSE; that is, it has the highest accuracy. A high-precision model can ensure that the model can be applied to the field of EMC, thereby ensuring the accuracy of the high-frequency aging model based on the high-frequency model.

B. High-Frequency Aging Model Prediction

In practice, the internal structure of the X-type capacitor and the Y-type capacitor is usually unknown. A model prediction

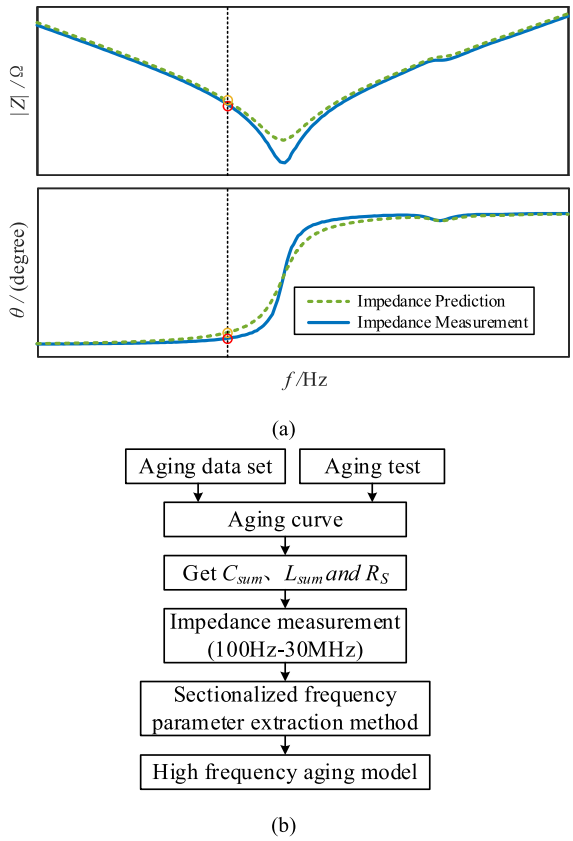

Fig. 37. Model aging prediction method. (a) Schematic diagram. (b) Method flow chart.

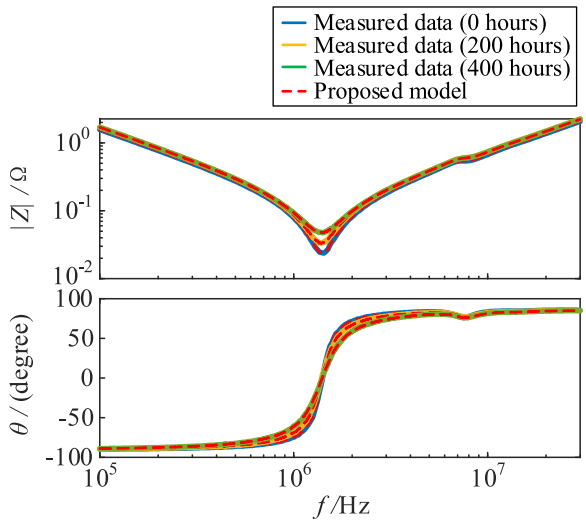

Fig. 38. High-frequency aging model prediction for X-type capacitor.

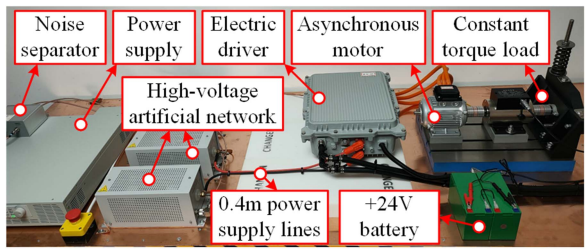

Fig. 39. 5 kW permanent magnet synchronous motor experiment platform.

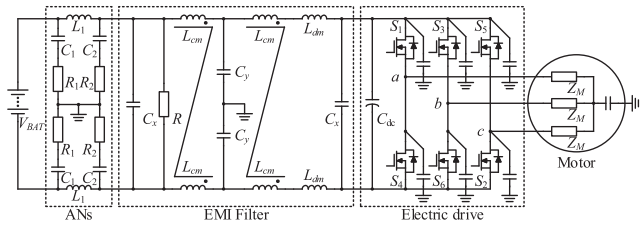

Fig. 40. Schematic diagram of the EMI measurement experiment.

method for practical applications is proposed in this article. The method is shown in Fig. 37. After an impedance measurement (100 Hz–30 MHz), the initial values of the individual parameters can be determined. At this time, the impedance of the model at 1 kHz can be obtained through the datasheet or the aging test data set. Based on (14), two equations of the real part and imaginary part can be established, and then the values of C_{sum}, L_{sum}, and R_S, can be obtained, and then the aging law of its impedance characteristics can be predicted.

Based on the earlier, the transformation law of the high-frequency impedance characteristics of the X-type capacitor with aging can be obtained. The impedance of capacitors with different aging levels is measured, and the measured data are compared with the impedance results calculated at different aging times according to the proposed aging model, as shown in Fig. 38. It can be seen that the proposed model can accurately predict the impedance change of the X-capacitor within 600 h.

C. Prediction of EMI Spectrum by EMI Filter Affected by Aging

In this article, a 5-kW motor experiment platform is built to verify the practicability of the model, as shown in Fig. 39. And the schematic diagram of the experiment is shown in Fig. 40. The motor driver is placed outside the ambient temperature chamber as the load of the EMI filter, and the EMI filter subjected to environmental stress and electrical stress continues to age.

Through the aforementioned Table VI, the predicted CM insertion loss and DM insertion loss of the EMI filter are shown in Fig. 41. Based on the EMI noise measurement of CISPR25, it can be seen that the performance of the DM filter is degraded due to the aging of the X-type capacitor, which is consistent with the prediction of the DM insertion loss of the EMI filter. Correspondingly, the CM noise suppression function of the EMI filter is mainly achieved by the CM inductor. The CM inductor is less affected by electrical stress and thermal stress, so the CM insertion loss of the EMI filter is less reduced, and ultimately the CM noise spectrum has less influence. Then predict the failure time of the EMI filter due to aging, as shown in Table VIII.

It can be seen that after the aging of the motor driver for 400 h, the conduction emission EMI exceeds the standard, which is consistent with the model proposed in this article, as shown in Fig. 42.

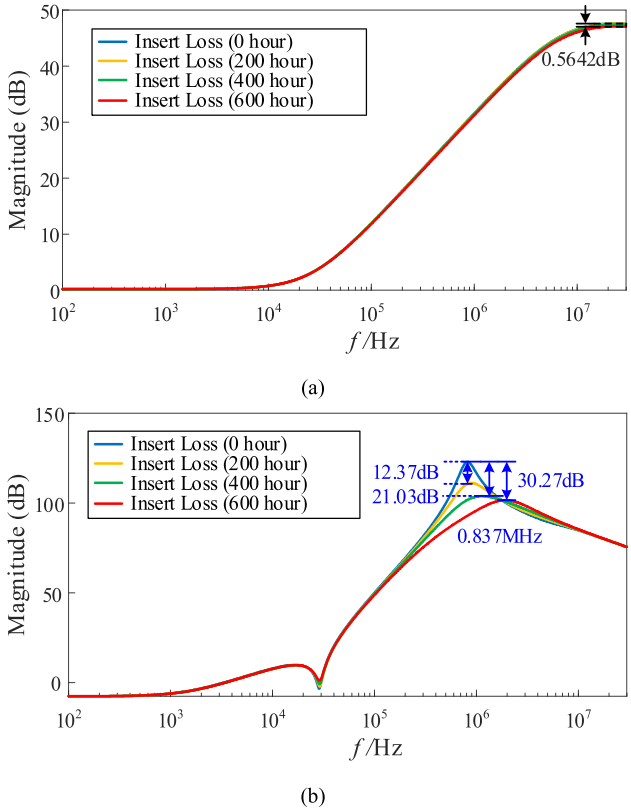

Fig. 41. Aging prediction of EMI filter. (a) CM insertion loss. (b) DM insertion loss.

TABLE VIII
PREDICT RESULTS OF THE FAILURE TIME OF THE EMI FILTER DUE TO AGING WITH DIFFERENT MODELS

Models	Failure time /hour	Min failure time /hour	Max failure time /hour
RC model	1252.2	1000.2	1644.7
RLC model	501.5	420.4	602.9
Proposed model	383.1	354.8	420.2

It can be seen that after the motor driver is aged for 400 h, the conducted emission EMI exceeds the standard, as shown in Fig. 22. The EMI filter DM suppression EMI failure time prediction calculation results fall within the calculation range of the prediction model proposed in this article. At the same time, at 200 h, the experimentally measured DM conduction EMI amplitude increases by 10.61 dBμV, which is 12.37 dB attenuation compared with the theoretically calculated insertion loss. It is consistent; at 400 h, the experimentally measured DM conduction EMI amplitude increases by 22.98 dBμV, which is consistent with the theoretically calculated DM insertion loss attenuation of 21.03 dB. At the same time, the experimental measurement of CM EMI is hardly affected by aging, which is consistent with the predicted insertion loss change of 0.5642 dB. The above-mentioned experiments verify the effectiveness and accuracy of the proposed model.

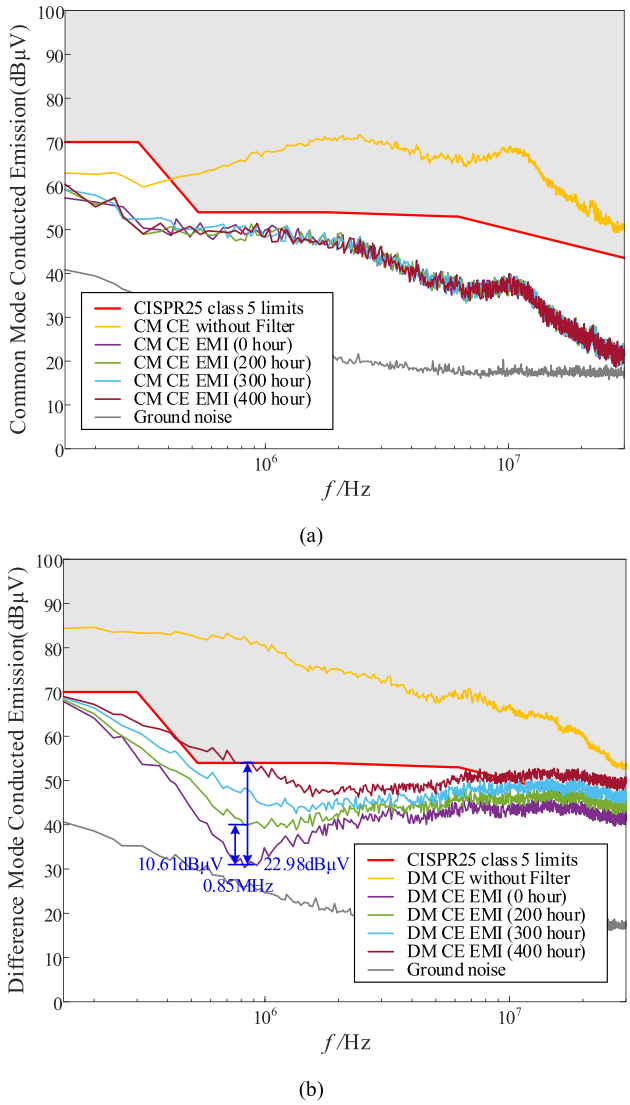

Fig. 42. Aging prediction of conducted emission EMI noise spectra. (a) CM EMI noise spectra. (b) DM EMI noise spectra.

VII. CONCLUSION

This article establishes a lumped parameter high-frequency aging model based on electromagnetic field analysis for passive electronic components in EMI filters. The characteristics of this article are organized as follows:

1) The proposed model explains the law of impedance degradation of passive devices affected by aging in the frequency range of 150 kHz–30 MHz, the goodness of fit of impedance amplitude and argument angle, and the adjusted R square is greater than 0.99.
2) The proposed model establishes a high-frequency aging model within the 95% confidence interval, which can effectively describe the changing trend of passive devices affected by aging.
3) The proposed parameter extraction method only needs one high-frequency impedance measurement to complete the

aging prediction of its impedance, which is suitable for EMC analysis considering aging and provides a full life cycle EMC design for data centers and EVs.

REFERENCES

[1] C. R. Paul, "EMC requirements for electronic systems," in *Introduction to Electromagnetic Compatibility*, 2nd ed., Hoboken, NJ, USA: Wiley, 2006, pp. 49–89.

[2] S. Maniktala, "EMI standards and measurements," in *Switching Power Supplies A-Z*, 2nd ed., Oxford, U.K.: Elsevier, 2012, pp. 597–620.

[3] S. Mocevic, V. Mitrovic, J. Wang, R. Burgos, and D. Boroyevich, "Gate-driver integrated junction temperature estimation of SiC MOSFET modules," *IEEE J. Emerg. Sel. Topics Power Electron.*, vol. 10, no. 5, pp. 4965–4980, Aug. 2021, doi: 10.1109/JESTPE.2021.3108442.

[4] H. Liu, T. Claeys, D. Pissoort, and G. A. E. Vandenbosch, "Prediction of capacitor's accelerated aging based on advanced measurements and deep neural network techniques," *IEEE Trans. Instrum. Meas.*, vol. 69, no. 11, pp. 9019–9027, Nov. 2020, doi: 10.1109/TIM.2020.3001368.

[5] B. Song, J. Chin, D. Kim, K. Hwang, and M. Lim, "Temperature estimation using lumped-parameter thermal network with piecewise stator-housing modules for fault-tolerant brake systems in highly automated driving vehicles," *IEEE Trans. Intell. Transp. Syst.*, vol. 22, no. 9, pp. 5819–5832, Sep. 2021, doi: 10.1109/TITS.2021.3091621.

[6] C. Stancu et al., "Thermal lifetime calculation of capacitor insulation using the activation energy method," *IEEE Trans. Compon., Packag., Manuf. Technol.*, vol. 10, no. 10, pp. 1647–1656, Oct. 2020, doi: 10.1109/TCPMT.2020.3019275.

[7] NASA Open Data, "Physics of failure models for capacitor degradation in DC–DC converters," *Distributed by Dashlink*, Jan. 29, 2020. Accessed: Nov. 24, 2022. [Online]. Available: https://data.nasa.gov/dataset/Physics-of-Failure-Models-for-Capacitor-Degradatio/5b6a-q3i8

[8] K. Yao, W. Tang, W. Hu, and J. Lyu, "A current-sensorless online ESR and C identification method for output capacitor of buck converter," *IEEE Trans. Power Electron.*, vol. 30, no. 12, pp. 6993–7005, Dec. 2015, doi: 10.1109/TPEL.2014.2383436.

[9] Film Capacitors General technical information, *TDK Co.*, Jun. 2018. [Online]. Available: https://www.tdk-electronics.tdk.com/download/530754/480aeb04c789e45ef5bb9681513474ba/pdf-generaltechnicalinformation.pdf

[10] B. Wang, J. Meng, and P. Zhao, "Aging condition monitoring for aluminum electrolytic capacitor in variable speed drives," *IEEE Trans. Power Electron.*, vol. 37, no. 4, pp. 4564–4574, Apr. 2022, doi: 10.1109/TPEL.2021.3121813.

[11] Y. Diab, P. Venet, H. Gualous, and G. Rojat, "Self-discharge characterization and modeling of electrochemical capacitor used for power electronics applications," *IEEE Trans. Power Electron.*, vol. 24, no. 2, pp. 510–517, Feb. 2009, doi: 10.1109/TPEL.2008.2007116.

[12] H. Yang, "Dependence of supercapacitor Peukert constant on voltage, aging, and temperature," *IEEE Trans. Power Electron.*, vol. 34, no. 10, pp. 9978–9992, Oct. 2019, doi: 10.1109/TPEL.2018.2890392.

[13] NASA Open Data, "Accelerated aging experiments for capacitor health monitoring and prognostics," *Distributed by Dashlink*, Jan. 29, 2020. Accessed: Nov. 24, 2022. [Online]. Available: https://data.nasa.gov/dataset/Accelerated-Aging-Experiments-for-Capacitor-Health/ay2e-c66a

[14] J. Wei, H. Feng, and L. Ran, "Integrated design for lifetime extension and ESR monitoring of hybrid DC link in solid-state transformer from the perspective of high-frequency ripple current," *IEEE Trans. Power Electron.*, vol. 37, no. 12, pp. 15583–15593, Dec. 2022, doi: 10.1109/TPEL.2022.3199499.

[15] A. El Mejdoubi, A. Oukaour, H. Chaoui, H. Gualous, J. Sabor, and Y. Slamani, "Prediction aging model for supercapacitor's calendar life in vehicular applications," *IEEE Trans. Veh. Technol.*, vol. 65, no. 6, pp. 4253–4263, Jun. 2016, doi: 10.1109/TVT.2016.2539681.

[16] C. Lv, J. Liu, and Y. Zhang, "A data-driven method for anomaly detection and aging model parameter estimation of capacitors based on condition monitoring," *Microelectronics Rel.*, vol. 138, Nov. 2022, Art. no. 114646.

[17] D. Li, S. Li, S. Zhang, J. Sun, L. Wang, and K. Wang, "Aging state prediction for supercapacitors based on heuristic Kalman filter optimization extreme learning machine," *Microelectronics Rel.*, vol. 138, Nov. 2022, Art. no. 114646.

[18] H. Zhao et al., "Rethinking basic assumptions for modeling parasitic capacitance in inductors," *IEEE Trans. Power Electron.*, vol. 37, no. 7, pp. 8281–8289, Jul. 2022, doi: 10.1109/TPEL.2021.3139682.

[19] A. Eroglu, "Complete modeling of toroidal inductors for high power RF applications," *IEEE Trans. Magn.*, vol. 48, no. 11, pp. 4526–4529, Nov. 2012, doi: 10.1109/TMAG.2012.2201922.

[20] K. Takahashi, Y. Murata, Y. Tsubaki, T. Fujiwara, H. Maniwa, and N. Uehara, "Simulation of shielding performance against near field coupling to EMI filter for power electronic converter using FEM," in *Proc. Int. Symp. Electromagn. Compat. - EMC Europe*, 2016, pp. 716–721, doi: 10.1109/EMCEurope.2016.7739152.

[21] H. Huang and T. Lu, "A cancelation method of mutual inductance between capacitors in EMI filter," *IEEE Trans. Power Electron.*, vol. 37, no. 10, pp. 11974–11984, Oct. 2022, doi: 10.1109/TPEL.2022.3173082.

[22] W. Su, H. Li, Z. Yang, and B. Zhang, "Research and modeling on the characteristic changes of EMI filter passive components under the influence of aging," *Chin. J. Elect. Eng.*, vol. 8, no. 3, pp. 2–11, Sep. 2022, doi: 10.23919/CJEE.2022.000021.

[23] *Vehicles, Boats and Internal Combustion Engines - Radio Disturbance Characteristics - Limits and Methods of Measurement for the Protection of On-Board Receivers*, CISPR25-Edition 5.0, Dec. 2021.

[24] P. Pieters, *Integration of Passive Devices, Encyclopedia of Materials: Science and Technology*. Oxford, U.K.: Elsevier, 2001, pp. 6769–6776.

[25] General Technical Information of Film Capacitors, Vishay Intertechnology Inc., Mar. 2022. [Online]. Available: https://www.vishay.com/docs/26033/gentechinfofilm.pdf

[26] D. K. Cheng, *Field and Wave Electromagnetics*. Noida, India: Pearson Education India, 1989.

[27] S. V. Suraci, D. Fabiani, K. Sipilä, and H. Joki, "Filler impact analysis on aging of crosslinked polyethylene for nuclear applications through dielectric spectroscopy," in *Proc. IEEE Conf. Elect. Insul. Dielectric Phenomena*, 2019, pp. 166–169.

[28] C. J. Kaiser, "Plastic film capacitors," in *The Capacitor Handbook*. Berlin, Germany: Springer, 2012.

[29] K. Nabors, S. Kim, and J. White, "Fast capacitance extraction of general three-dimensional structures," *IEEE Trans. Microw. Theory Techn.*, vol. 40, no. 7, pp. 1496–1506, Jul. 1992, doi: 10.1109/22.146331.

[30] T. Sakurai and K. Tamaru, "Simple formulas for two- and three-dimensional capacitances," *IEEE Trans. Electron Devices*, vol. 30, no. 2, pp. 183–185, Feb. 1983, doi: 10.1109/T-ED.1983.21093.

[31] F. Salomez, A. Videt, and N. Idir, "Modeling and minimization of the parasitic capacitances of single-layer toroidal inductors," *IEEE Trans. Power Electron.*, vol. 37, no. 10, pp. 12426–12436, Oct. 2022, doi: 10.1109/TPEL.2022.3177642.

[32] S. Maniktala, "Component ratings, stresses, reliability, and life," in *Switching Power Supplies A-Z*, 2nd ed., Oxford, U.K.: Elsevier, 2012, ch. 16, sec. 1, pp. 241–280.

[33] Mathworks, Evaluating Goodness of Fit, Aug. 30, 2023. [Online]. Available: https://ww2.mathworks.cn/help/curvefit/evaluating-goodness-of-fit.html

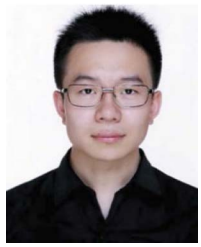

Wenzhe Su (Student Member, IEEE) received the B.E. degree in electrical engineering from Shanxi University, Taiyuan, China. He is currently working toward the Ph.D. degree in electrical engineering with Beijing Jiaotong University, Beijing, China.

From 2018 to 2019, he was a Visiting Scholar with The University of Western Australia, Crawley, Australia, where he worked on renewable energy management in power systems. His current research interests include EMC of power electronic systems and electromagnetic interference analysis of electric vehicle electronic systems.

Mr. Su is a Chair of the China IEEE Power Electronics Society, Beijing Jiaotong University, in 2021.

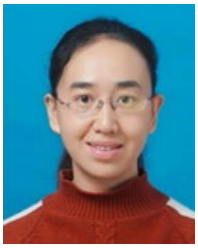

Hong Li (Senior Member, IEEE) received the B.Sc. degree in electrical engineering from Taiyuan University of Technology, Taiyuan, China, in 2002, the M.Sc. degree in electrical engineering from South China University of Technology, Guangzhou, China, in 2005, and the Ph.D. degree in electrical engineering from Fernuniversität in Hagen, Hagen, Germany, in 2009.

She is currently a Full Professor with the School of Electrical Engineering, Beijing Jiaotong University, Beijing, China. She has authored or coauthored 1 book, 68 journal papers, and 61 conference papers. She has also authorized 30 patents. Her research interests include nonlinear modeling, analysis and its applications, EMI suppressing methods for power electronic systems, and wide bandgap power devices and applications.

Dr. Li is an Associate Editor for IEEE TRANSACTIONS ON INDUSTRIAL ELECTRONICS, IEEE OPEN JOURNAL OF INDUSTRIAL ELECTRONICS SOCIETY, and *Chinese Journal of Electrical Engineering*, and the Vice Chairman of the Electromagnetic Compatibility Specialized Committee in China Power Supply Society.

Changlin Ji received the B.E. degree in electrical engineering and intelligent control from Shanghai Maritime University, Shanghai, China, and the master's degree in electrical engineering from Beijing Jiaotong University, Beijing, China.

She is currently a Hardware Engineer with Active Safety Technology – Steering Electronics Department from ZF Automotive Technologies (Shanghai) Company, Ltd., Shanghai, China. Since 2019, she is responsible for Electrical Power System products as a Technical Project Manager for several projects in terms of automotive, focusing on circuit analysis and electronics characteristics verification. Her current research interests include steering electronics design and related EMC and electrical and environmental tests of electrical power pack and system.

Zuoxing Wang (Student Member, IEEE) was born in Shanxi, China, in 1994. He received the B.S. degree from China University of Mining and Technology, Beijing, China, in 2016, the M.S. degree in 2019 from Beijing Jiaotong University, Beijing, China, where he is currently working toward the Ph.D. degree in electrical engineering.

His research interests include EMC of power electronic systems and modular multilevel converters.

Xueyang Liu received the bachelor's degree in electrical engineering from Xi'an University of Technology, Xi'an, China. She is currently working toward the master's degree in electrical engineering with Beijing Jiaotong University, Beijing, China.

Her current research direction is electromagnetic compatibility research of power electronic systems.

Baihua Zhang received the B.E. degree from Beijing Jiaotong University, Beijing, China, in 2013, and the M.E. and Ph.D. degrees in electrical and electronic engineering from Kyushu University, Fukuoka, Japan, in 2016 and 2019, respectively.

In 2019, he joined the Institute of Engineering Thermophysics, Chinese Academy of Sciences. He is also the Technical Director and Authorized Signatory of EMC Laboratory, Integrated Test Center of UAV Research Institute, Qingdao Institute of Aeronautical Technology. His research interests include EMC tests, EMI modeling, power electronics, and flight control and avionics systems of UAVs.